



저작자표시-비영리-변경금지 2.0 대한민국

이용자는 아래의 조건을 따르는 경우에 한하여 자유롭게

- 이 저작물을 복제, 배포, 전송, 전시, 공연 및 방송할 수 있습니다.

다음과 같은 조건을 따라야 합니다:



저작자표시. 귀하는 원저작자를 표시하여야 합니다.



비영리. 귀하는 이 저작물을 영리 목적으로 이용할 수 없습니다.



변경금지. 귀하는 이 저작물을 개작, 변형 또는 가공할 수 없습니다.

- 귀하는, 이 저작물의 재이용이나 배포의 경우, 이 저작물에 적용된 이용허락조건을 명확하게 나타내어야 합니다.
- 저작권자로부터 별도의 허가를 받으면 이러한 조건들은 적용되지 않습니다.

저작권법에 따른 이용자의 권리는 위의 내용에 의하여 영향을 받지 않습니다.

이것은 [이용허락규약\(Legal Code\)](#)을 이해하기 쉽게 요약한 것입니다.

[Disclaimer](#)

공학석사 학위논문

**Numerical study of surface plasmon polaritons
scattering at a planar metal–dielectric interface
by an embedded dielectric nanocube**

금속 내부의 나노정육면체에 의한 평면
금속-유전체 계면 표면 플라즈몬의 산란 연구

2017년 2월

서울대학교 융합과학기술대학원

융합과학부 나노융합전공

이 서 준

**Numerical study of surface plasmon polaritons
scattering at a planar metal–dielectric interface
by an embedded dielectric nanocube**

지도교수 김 창 순

이 논문을 공학석사 학위논문으로 제출함

2017년 2월

서울대학교 융합과학기술대학원

융합과학부 나노융합전공

이 서 준

이서준의 석사학위논문을 인준함

2017년 2월

위 원 장 송 윤 규 (인)

부위원장 김 창 순 (인)

위 원 김 연 상 (인)

Abstract

Numerical study of surface plasmon polaritons scattering at a planar metal–dielectric interface by an embedded dielectric nanocube

Seojun Lee

Program in Nano Science and Technology

Graduate School of Convergence Science and Technology

Seoul National University

Surface plasmon polaritons (SPPs) are localized electromagnetic waves propagating along a planar metal–dielectric interface. SPPs have drawn much attention in a variety of applications, such as light-emitting diodes, solar cells, Raman scattering, chemical or biological sensors, and integrated plasmonic circuits since they are localized electromagnetic waves on a metallic surface with higher local field density. As they have been applied in many applications, the in- and out-coupling of SPPs become important to efficiently excite SPP modes (in-coupling of SPPs), convert SPP modes into far-field radiating modes, electromagnetic waves propagating away from the metal surface to which SPPs are confined (out-coupling of SPPs), or manipulate SPPs (reflection or transmission). Particularly, efficient scattering of SPPs into the far-field

radiating modes or reflected or transmitted SPPs is demanded in areas such as thin-film spectroscopy, integrated plasmonic devices, or organic light-emitting diodes (OLEDs).

In this numerical study, it is investigated that how SPPs at a planar metal–dielectric interface are scattered by a dielectric nanocube embedded in the metal layer. The scattering properties of the embedded nanocube in terms of cross sections of scattering and absorption, scattering patterns, reflection, and transmission are numerically analyzed employing three-dimensional finite element method based simulations. It is confirmed that this embedded nanocube structural system is capable of wavelength-selective SPPs scattering dependent on the size of the nanocube due to the plasmonic resonant modes that are excited in the nanocube.

Moreover, the correlation between the scattering properties of the embedded nanocube and the characteristics of the plasmonic resonant modes found in the embedded nanocube is discussed, showing that a specific plasmonic mode, which similarly appears in each of different-sized nanocubes, is responsible for strong scattering of SPPs. Along with the strong outcoupling of SPPs, the strong reflection also occurs when resonant modes of the embedded nanocube are excited, while the transmission decreases. In addition, the scattering patterns of the scattered waves out-coupled by the embedded nanocube are also discussed.

With further development, this study would contribute to efficient scattering of SPPs at a planar interface, which can increase the performance of integrated plasmonic devices and, especially, the efficiency of OLEDs by

outcoupling of SPPs into the far field radiating modes by collection of embedded dielectric nanocubes with an appropriately chosen size distribution.

.....

Keywords: surface plasmon polariton, scattering, integrated plasmonic circuit, nanocavity, OLED

Student Number: 2014-24880

Contents

Abstract	1
Contents	4
List of Figures	5
1. Introduction	8
2. Modulation of Surface Plasmon Polaritons	
2.1 Surface plasmon polaritons	11
2.2 Conventional modulation methods of surface plasmon polaritons: waveguides, reflectors, filters, and out-couplers	17
3. Results and Discussion	
3.1 Simulation structure and method	25
3.2 Scattering of surface plasmon polaritons into the far field	29
3.3 Absorption characteristics	44
3.4 Reflection and transmission	48
4. Conclusion	53
Bibliography	55
초록 (국문)	60

List of Figures

Figure 2.1.1 A single p-polarized plane wave at the interface ($z = 0$) between media 1 and 2 with relative permittivity ϵ_1 and ϵ_2	12
Figure 2.1.2 The dispersion relation between the propagation constant (k_x) and the angular frequency of electromagnetic surface waves at the interface of Ag–Air; $\epsilon_1(\omega) = \epsilon_{\text{Ag}}(\omega)$ and $\epsilon_2 = \epsilon_{\text{Air}} = 1$. Blue line represents the light line.....	16
Figure 3.1.1 Schematic diagrams of the simulation structure showing that SPP waves (red) are excited from the left to the right, propagating along the x axis, while a TiO ₂ nanocube ($w = 100, 80,$ or 60 nm) is embedded in the Ag layer. The structure is shown in three-dimensional (a) and two-dimensional (b) views, where θ and φ represent the polar and azimuthal angles, respectively.....	27
Figure 3.1.2 Frequency-dependent relative permittivity (ϵ) of the metal layer (Ag) and the embedded dielectric nanocube (TiO ₂) as a function of a wavelength in vacuum (λ) used in this study.....	28
Figure 3.2.1 The S_{sca} spectra of the embedded TiO ₂ nanocube with $w = 100, 80,$ and 60 nm as a function of λ	31
Figure 3.2.2 The surface charge densities (σ) distribution (a) and E_x field profile (c) of the 100-nm nanocube corresponding to the S_{sca} peak at $\lambda = 680$ nm (λ_1). In (b), the σ distribution over the embedded nanocube of the eigenmode found at $\lambda = 674$ nm.	33
Figure 3.2.3 The surface charge densities (σ) distribution of the 100-nm nanocube corresponding to the S_{sca} peaks at $\lambda = 640$ (λ_2) and 540 nm (λ_2) are shown in (a) and (b), respectively. In (c) and (d), the σ distributions corresponding to the eigenmodes found at $\lambda = 634$ and 539 nm are shown, respectively.....	34
Figure 3.2.4 The E_x (a) and E_z (b) field profiles of the 100-nm nanocube for λ	

= 640 nm (λ_2), where a S_{sca} peak is found..... 35

Figure 3.2.5 The distribution of surface charge densities (σ) of the embedded nanocube with $w = 80$ and $w = 60$ when the S_{sca} peaks arise: (a) $w = 80$ nm and $\lambda = 640$ nm (the dipolar-like mode), (b) $w = 60$ nm and $\lambda = 600$ nm (the dipolar-like mode), (c) $w = 80$ nm and $\lambda = 600$ nm (the 1st higher mode), (d) $w = 60$ nm and $\lambda = 570$ nm (the 1st higher mode), (e) $w = 80$ nm and $\lambda = 520$ nm (the 2nd higher mode), and (f) $w = 60$ nm and $\lambda = 500$ nm (the 2nd higher mode). 38

Figure 3.2.6 Characteristics of the additional resonant mode in the 60-nm nanocube. The distribution of surface charge density (σ) for $\lambda = 660$ nm is shown in (a), which is obtained from the SPP scattering simulation; the σ distribution corresponding to the eigenmode found at $\lambda = 675$ nm via the eigenmode calculation is shown in (b). The E_x and E_z profiles in this case are also shown in (c) and (d), respectively. 40

Figure 3.2.7 The far-field scattering patterns for the SPP scattering by the embedded nanocube. The scattering patterns for $w = 100$ nm when the dipolar-like (a), 1st higher (b), and 2nd higher (c) modes are excited by incident SPPs are shown. In (d), the scattering pattern in the case of excitation of the additional resonant mode (for $w = 60$ nm and $\lambda = 660$ nm) is also shown. The direction of far field scattering is represented by the polar (θ , as lines) and azimuthal (φ , as dotted lines) angles. 43

Figure 3.3.1 The S_{abs} spectra of the embedded TiO₂ nanocube with $w = 100, 80,$ and 60 nm as a function of λ 46

Figure 3.3.2 The dissipated power density inside the metal layer (Ag) including the embedded nanocube (TiO₂) and the thin metal region (indicated by the white arrow), which is considered in the absorption calculation, plotted in the xz -plane bisecting the nanocube (a) and in the xy -plane located at $z = -15$ nm (b) in the case of $w = 100$ nm and $\lambda = 650$ nm. 47

Figure 3.4.1 Calculated spectra of R (green) and T (blue) compared with the values of S_{sca} (black) of the embedded nanocube for $w = 100, 80,$ and 60

nm.	50
Figure 3.4.2 $ \mathbf{E} ^2$ distribution (log scale) over the xy plane at $z = 1$ nm in the case of the maximum reflectance (when $w = 100$ nm and $\lambda = 640$ nm). 51	
Figure 3.4.3 Local field enhancement ($ \mathbf{E} ^2 / \mathbf{E}_0 ^2$) on the surface of the metal layer due to the embedded nanocube with $w = 60$ nm at $\lambda = 680$ nm. 52	

1. Introduction

Surface plasmon polaritons (SPPs) are localized electromagnetic waves propagating along a metal–dielectric interface. In general, SPPs are excited by electromagnetic waves that are of a specific frequency and momentum appropriate to resonate with interior charges in a metal. When such electromagnetic waves resonantly couple with the charges in the metal, collective oscillations of charges along the metallic surface arise, producing electromagnetic waves decaying exponentially from the metal–dielectric interface. Since the wavelength of SPP waves is shorter than that of electromagnetic waves inducing the SPPs, SPPs can overcome the diffraction limit. Also, since SPPs are propagating electromagnetic waves tightly confined to the metallic surface, localization of electromagnetic fields can also be realized with higher local field density at the metallic surface. With these unique properties, SPPs are currently applied to many sub-wavelength applications, such as integrated plasmonic circuits (waveguides [1,2], beam splitters [3], and switches [4]), ultra-compact lasers [5], nano-scaled lithography [6], solar cells [7], and organic light-emitting diodes (OLEDs) [8].

To maximize the benefits from those unique properties of SPPs in applications, SPPs modulating methods to realize controlled SPPs reflection, transmission, and outcoupling into “far-field” radiating modes, electromagnetic waves propagating away from the metallic surface, are required. These can be achieved by scattering SPPs at the interface, which would allow for controlling the amount of SPPs propagating along the surface, SPPs reflections and

transmission, outcoupling of SPPs, and possibly favorable directionality to SPPs. Although some theoretical works of SPPs scattering has been done by Cullen [9], Davis and Leppington [10], and Pincemin [11], these are based on assumptions such as limiting to a perfect conductor, impedance boundary condition, or an infinite rectangular cylinder structure. Few experimental works demonstrating SPPs scattering also have been reported to date, yet they require some structural modifications on the metal surface [12, 13] to out-couple, reflect, or filter SPPs, resulting in a non-planar interface. Besides, these works are limited to certain structural systems and quantitative analyses, demanding a flexible, systematic approach to investigate SPPs scattering.

Therefore, in this study, scattering of SPPs whose wavelengths are in the visible range in vacuum at a planar metal–dielectric interface by a dielectric nanocube embedded in a metal layer is numerically investigated employing three-dimensional finite-element method (FEM) based simulations (COMSOL). When a SPP-modes supporting system, such as a planar metal–dielectric structure, is altered by an additional object such as a dielectric nanocube in a metal layer, SPPs are no longer able to be sustained and then they are scattered into the far field radiating modes (hereafter, referred to as the far field), and reflected or transmitted SPPs still bound at the metallic surface. Since a numerical approach is not limited by a specific structural system or experimental difficulties to accurately measure quantitative properties such as total power of scattered waves and incident SPP waves, it is an appropriate mean to perform an thorough investigation of SPPs scattering specifically in terms of SPPs scattering into the far field, far-field scattering patterns,

absorptions, and SPPs reflection and transmission. Together with the frequency-dependent relative permittivity for the metal layer (Ag) and the dielectric nanocube (anatase titanium dioxide, TiO₂), it is confirmed that this embedded nanocube structural system is capable of wavelength-selective SPPs manipulation, such as outcoupling of SPPs into the far field, reflecting, and filtering (selective transmission), dependent on the size of the embedded nanocube due to the plasmonic resonant modes excited in the embedded nanocube. In addition, each plasmonic resonant mode in the embedded nanocube excited is attributed with a different far-field scattering pattern observed. With further study, it would contribute to efficient scattering of SPPs at a planar interface, which can increase the performance of integrated plasmonic devices. Moreover, in OLEDs, the efficiency of devices could be significantly increased by scattering SPP modes, which arise from near-field coupling of emitting molecules due to the close proximity of the emissive layer to the metallic surface and therefore result in huge loss of power emitted by the emitting molecules [14], into the far field employing collection of embedded dielectric nanocubes with an appropriately chosen size distribution.

2. Modulation of Surface Plasmon Polaritons

2.1 Surface plasmon polaritons

Surface plasmon polaritons (SPPs) are confined electromagnetic waves propagating along a metallic surface, resulting from collective charge oscillations at the metallic surface induced by coupling between charges in the metal and photons. It is a resonance phenomenon arising in the case when electromagnetic waves are incident on a metal with a specific frequency and momentum appropriate to resonant with the natural oscillations of charges in the metal. There are some unique properties in SPPs: (i) spatial confinement near a metal surface, (ii) higher local field density, (iii) un-limitation by the diffraction limit, (iv) propagation along a metallic surface. With these beneficial characteristics for sub-wavelength applications, SPPs are applied to plasmonic integrated circuits, waveguides, high-resolution lithography, lasers, and organic electronics. In this section, wavevectors and field equations of SPPs are analytically derived and then discussed qualitatively. We consider a system consisting of two medias with an interface at $z = 0$ as shown in Fig. 2.1.1. Media 1 and 2 are characterized by a frequency-dependent relative permittivity, ϵ_1 and ϵ_2 , respectively. It is assumed that the media 2 is a kind of lossless dielectric material, indicating that the relative permittivity of media 2 is real. On the other hand, media 1 is a metal with a complex relative permittivity.

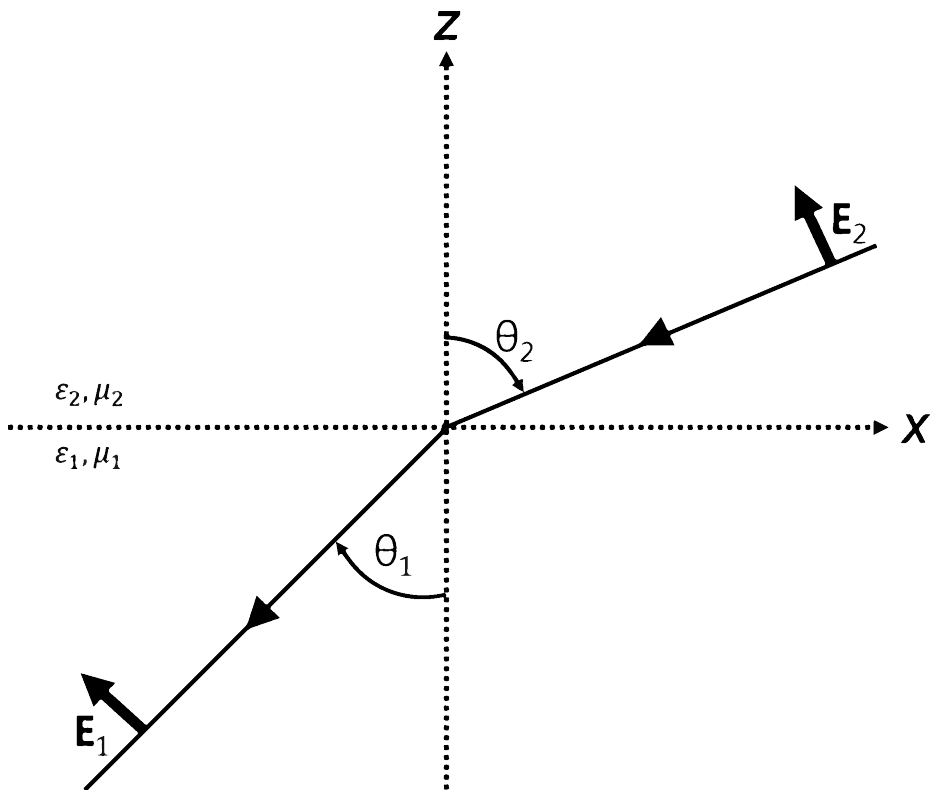


Figure 2.1.1 A single p-polarized plane wave at the interface ($z = 0$) between media 1 and 2 with relative permittivity ϵ_1 and ϵ_2 .

In order to define SPPs in the system, it is necessary to find homogenous solutions of the Maxwell's equations that decay exponentially with increasing distance from the interface into both half spaces [15]. Since there is no solution for s-polarization, it is only necessary to consider p-polarized waves in both half spaces. SPP are solutions of the wave equation with the angular frequency (ω),

$$\nabla \times \nabla \times \mathbf{E}(\mathbf{r}, \omega) - \frac{\omega^2}{c^2} \varepsilon(\mathbf{r}, \omega) \mathbf{E}(\mathbf{r}, \omega) = 0, \quad (2.1)$$

where $\varepsilon(\mathbf{r}, \omega) = \varepsilon_1(\mathbf{r}, \omega)$ for $z < 0$ and $\varepsilon(\mathbf{r}, \omega) = \varepsilon_2(\mathbf{r}, \omega)$ for $z > 0$. The possible solution that is of p-polarized waves locally confined in close proximity to the metal surface can be written as

$$E_j = \begin{Bmatrix} E_{j,x} \\ 0 \\ E_{j,z} \end{Bmatrix} e^{-ik_{j,z}z} e^{-ik_x x - i\omega t}, \quad j = 1, 2. \quad (2.2)$$

The momentum has to be conserved as follows

$$k_x^2 + k_{j,z}^2 = \varepsilon_j k^2, \quad j = 1, 2 \quad (2.3)$$

where k describes the wavevector in vacuum. Since the both media 1 and 2 are source free ($\nabla \cdot \mathbf{D} = 0$), a following relation needs to be satisfied as well

$$k_x E_{j,x} + k_{j,z} E_{j,z} = 0, \quad j = 1, 2. \quad (2.4)$$

According to the boundary conditions,

$$E_{1,x} = E_{2,x}, \quad (2.5)$$

$$\varepsilon_1 E_{1,z} = \varepsilon_2 E_{2,z} \quad (2.6)$$

are required, where $E_{j,x}$ and $E_{j,z}$ are the parallel, and perpendicular component of \mathbf{E} in each media, respectively ($j = 1, 2$). With (2.2), (2.4), and

(2.5), electric fields of SPPs in media 1 and 2 can be defined as follows

$$E_j = \begin{pmatrix} 1 \\ 0 \\ -k_x \\ k_{j,z} \end{pmatrix} e^{-ik_{j,z}z} e^{-ik_x x - i\omega t}, \quad j = 1, 2. \quad (2.7)$$

To determine wavevectors of SPPs in the system, a homogenous system of four equations for the four unknown field components formed together with (2.4), (2.5), and (2.6) is necessary to be solved. The determinant should be vanished as a condition required for a solution. It occurs when either $k_x = 0$, or

$$\varepsilon_1 k_{2,z} - \varepsilon_2 k_{1,z} = 0. \quad (2.8)$$

By combining (2.3) with (2.8), dispersion relations between the wavevectors and the angular frequency can be obtained as follows

$$k_x^2 = \frac{\varepsilon_1 \varepsilon_2}{\varepsilon_1 + \varepsilon_2} \left(\frac{\omega^2}{c^2} \right), \quad (2.9)$$

$$k_{j,z}^2 = \frac{\varepsilon_j^2}{\varepsilon_1 + \varepsilon_2} \left(\frac{\omega^2}{c^2} \right), \quad j = 1, 2. \quad (2.10)$$

For localized surface modes to be existed at the interface, it is shown that both the real part of $\varepsilon_1 \varepsilon_2$ and $\varepsilon_1 + \varepsilon_2$ should be negative, meaning that one of the media should have a large and negative real part of relative permittivity with a small imaginary part of relative permittivity, like the case of noble metals such as gold and silver. We now obtain electric fields and wavevectors that describe SPPs at the metal–dielectric interface. The properties of SPPs such as SPPs wavelength, propagation length, and decay lengths into both media can be discussed.

The wavelength (λ_{SPP}) and the 1/e propagation length (L_{SPP}) of the SPPs along the interface determined from the dispersion relation (2.9) are

$$\lambda_{SPP} = \frac{2\pi}{k'_x} \approx \sqrt{\frac{Re(\epsilon_1) + \epsilon_2}{Re(\epsilon_1)\epsilon_2}} \lambda_0 \quad (2.11)$$

$$L_{SPP} = \frac{1}{k''_x} \quad (2.12)$$

where $k'_x = Re(k_x)$, $k''_x = im(k_x)$, and λ_0 is the wavelength in vacuum. The 1/e intensity propagation length in the direction of propagation is $1/(2k''_x)$. The 1/e decay lengths into both media can be obtained from (2.10) as

$$L_z = \frac{1}{k''_{j,z}}, \quad j = 1, 2 \quad (2.13)$$

with $k_{j,z} = k'_{j,z} + ik''_{j,z}$. It is observed that since $Re(\epsilon_1)\epsilon_2 > Re(\epsilon_1) + \epsilon_2$ in the case of the metal–dielectric interface, λ_{SPP} is smaller than λ_0 , representing that SPPs can be used to sub-wavelength microscopy and lithography by overcoming the diffraction limit. The damping of SPPs in a direction of propagation is due to the Ohmic losses of the electrons associated in the SPP, resulting in heating of the metal. For example, with $\epsilon_2 = 1$ and a vacuum wavelength of 633 nm, the 1/e intensity propagation length is ~60 um and ~10 um for silver and gold, respectively. The characteristics of the localization of SPPs at the surface are confirmed from the large imaginary part of the normal wavevectors ($k''_{j,z}$). For instance, with the vacuum wavelength of 633 nm, the 1/e decay length according to (2.13) are 23 nm and 421 nm, and 28 nm and 328 nm, for silver–air and gold–air, respectively.

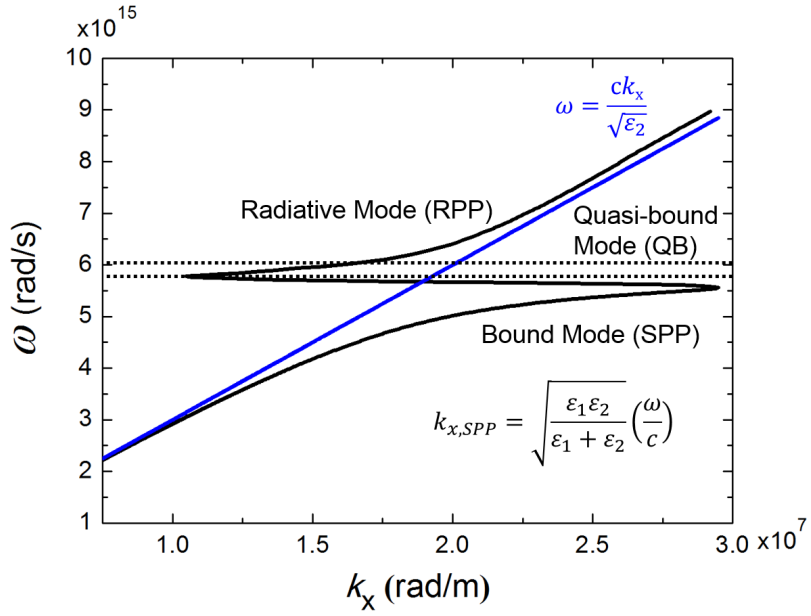


Figure 2.1.2 The dispersion relation between the propagation constant (k_x) and the angular frequency of electromagnetic surface waves at the interface of Ag–Air; $\epsilon_1(\omega) = \epsilon_{\text{Ag}}(\omega)$ and $\epsilon_2 = \epsilon_{\text{Air}} = 1$. Blue line represents the light line.

This indicates that the decay length into the dielectric is much longer than that into the metal, resulting in coupling to another metallic surface through the dielectric if there is another metallic surface. It is also noted that the comparatively shorter decay length into the metal is still enough to penetrate a thin metal film. Using a scanning tunneling optical microscope the decay of SPPs into the dielectric space can be experimentally observed [16]. It is shown in the dispersion relation that the propagation constant (k_x) of the SPPs is bigger than the wavevector of light in the dielectric media, indicating that the local enhancement of the fields is realized near the metallic surface (Fig. 2.1.2). Due to the fact that SPPs are induced from a strong coupling between photons and charges in the metal at the interface, it has increased momentum in a direction of the propagation, thus resulting in its local field enhancement. This beneficial characteristic is very useful in improving the Raman scattering, which is a powerful observation method for surface defects, structures, biomolecular, and so on.

2.2 Conventional modulation methods of surface plasmon polaritons

Surface plasmon polaritons draw interests from scientists since 1950s following the work done by Ritchie [17]. Its unique properties: i) spatial confinement to the metal surface, ii) higher local field density, iii) sub-wavelength scale. These enable SPPs to be considered as a key for realization of sub-wavelength signal processing, new light sources, highly sensitive sensors for biomolecules, nano-

scaled lithography, highly efficient solar cells, and magneto-optic data storage.

Among the promising applications of SPPs, specifically, active research for SPPs based sub-wavelength all-optical circuits is ongoing due to the potential of SPPs for concentrating and channeling light using sub-wavelength structures. Since modern electronics is, today, approaching to nano-scaled integrated circuits or chips, SPPs based signaling is one of the solutions that could realize sub-wavelength integrated circuits. In this section, research on basic components for the SPPs based signaling including SPPs waveguides, reflectors, filters, and out-couplers based on scattering are summarized.

SPPs Waveguides

Referring to Berini et al. [18], the structure of single or multiple thin metal films embedded in dielectric is proposed as SPPs waveguides. It is shown that the waveguides comprised of thin metal films embedded in dielectric can guide the near infrared SPPs ($\lambda_0 = 1550 \text{ nm}$) with maximum propagation lengths of $10,340 \text{ }\mu\text{m}$ (Au) and $13,582 \text{ }\mu\text{m}$ (Ag). It is the one of the best reported SPPs propagation lengths in the field of single-interface SPPs waveguides, raising the prospect of sub-wavelength circuitry, such as plasmonic integrated circuits.

To substantially reduce the loss incurred by the Ohmic loss in SPPs propagation along plasmonic waveguides, it is also proposed that a lattice of gold nanoparticles is also available as a plasmonic waveguide with less Ohmic loss [19]. In generally, since the more metallic volume induces the more Ohmic loss in propagating SPPs, a lattice of gold nanoparticles is suitable to reduce the

loss. With the pattern of gold nanoparticles, where the size of gold nanoparticles is laterally decreased from the center, the guiding of SPPs is feasible. Both waveguides introduced above not only have high-efficient SPPs coupling efficiency, but also are in scale of sub-wavelength, thus opening a way into converging with conventional electronic circuits.

SPPs reflectors

For SPPs reflectors, plasmonic Bragg reflectors are proposed. Referring to the work done by Liu et al. [20], finite array of periodic grooves on the two surfaces of metal–insulator–metal (MIM) waveguide is introduced as a plasmonic Bragg reflector. The periodic structure tailors appropriate photonic band gap, reflecting unfavorable SPPs. By filling the narrow slit of the structure with materials of higher refractive index, the bandgap can be widened. In addition, increasing the groove depth in the structure is also possible to widen the bandgap width.

Not only a periodic structure resulting in the photonic bandgap, but also an one-atom thick reflector for SPPs using graphene is proposed as well. Vakil and Engheta [21] introduce a straight-line mirror and a parabolic reflector with one-atom thickness to guide infrared SPPs on the graphene. Since the conductivity of the graphene can be tuned by doping, gate voltage, or chemical potential, it is shown that the graphene can act as like a metal if an appropriate method is employed to make the graphene have positive imaginary conductivity. Due to the fact that the electrical and optical properties can be tuned, non-uniform and inhomogeneous patterns of conductivity throughout the graphene is possible to

be formed. With the flexibility, the conductivity-patterned graphene is proposed as a new ultra-thin SPPs waveguide. Furthermore, using the platform, for infrared SPPs, one-atom-thick parabolic mirror is demonstrated using simulation.

SPPs filters

In the plasmonic integrated circuits, the controllability of passing or blocking certain frequencies is demanded, thus requiring the realization of SPPs filters. Lee and Lan [22] propose that employing strip cavities in a metal–insulator–metal plasmonic waveguide can lead to a band-stop plasmonic filter. The use of optical cavities embedded in the metal close to the metal–insulator interface allows us to use cavity effects, the resonance, thus possible for blocking specific resonant frequencies. Since the distance between the optical cavities and the interface is also in nano-scale, tunneling through the thin metal is feasible. It is observed that the longer the cavity is, the more red-shift in the blocking frequency is happened. In addition, it is also shown that the bandgap width is inversely proportional to the distance between the waveguide and the cavity. With different size of the cavities embedded in the metal, a plasmonic filter with multiple blocking frequencies in the metal–insulator–metal plasmonic waveguide is demonstrated using simulation.

The ring resonators are also considered as a key component for realization of all-optical devices. Especially in the metal–insulator–metal plasmonic gap waveguide, ring resonators are capable of bandpass filters, wavelength

multiplexers or de-multiplexers, and switches. Regarding to the work done by Hosseini and Massoud, a rectangular ring resonator is designed and numerically investigated as SPPs filters and directional couplers [23]. It is shown that the ring have a role of a cavity, resonating with specific frequency, thus acting as like a bandpass filter. The size of the ring resonator and the separation distance between the resonator and the waveguide determine the frequencies that are forbidden to transmit. It is also indicated that the anti-symmetric sized ring resonator suppresses one of the resonance mode, otherwise would have simultaneously occurred. Additionally placing a bridge between the resonator and the waveguide shifts the resonant frequency, allowing more flexibility in tuning the forbidden frequencies.

SPPs out-couplers

To realize sub-wavelength all-optical devices, the SPPs out-coupler is considered as a main component. With a well-designed SPPs out-coupler, it is possible to manipulate SPPs propagating in plasmonic waveguides in variety ways. It can have a role of a reflector, filter, directional coupler, and wavelength de-multiplexer. In this section theoretical and experimental work for SPPs out-couplers up to date are discussed.

By Pincemin and Maradudin [11], SPPs scattering properties are theoretically investigated when a rectangular dielectric rod is embedded in the metal. The structure that consists of a single metal–dielectric interface, where SPPs propagate along the surface. Using the approach of the Green's function and the volume-integral-equation, in this theoretical work, reflectance,

transmittance, and SPPs conversion efficiency into volume electromagnetic waves propagating away from the metal surface are numerically calculated. It also shows that with the information from the theoretical work for the far-field and the near field as well, it is feasible to obtain the dielectric constant of the defect underneath the surface, the dielectric rod embedded in the metal. Although in this research promising theoretical work is achieved for SPPs scattering modeling, it is limited to the case of an infinite-size rectangular rod embedded in the metal.

Another theoretical framework of SPPs scattering modeling also has been done by Evlyukhin [24]. In this study, finite-sized nanoparticles placed in dielectric media near the flat metallic surface, rather than the infinite-sized dielectric, are investigated in terms of the differential and total scattering cross-sections using the electromagnetic Green's tensor approach (GTA). Specifically, different SPPs scattering channels, elastic SPP to SPP scattering, SPP into far-field scattering, are calculated by the Green's function formalism. It also presents and compares with the result of using the point-dipole approximation (PDA), in general, being used to determine the scattering properties of an individual spherical particle. It is also confirmed that the scattering properties are strongly dependent on the size of the nanoparticle and the distance between the nanoparticle and the metallic surface. As a conclusion, the PDA approach is not enough to give quantitative agreement compared to experimental result without the GTA assistance, especially when frequencies under investigation are close to the resonance of the nanoparticle.

Not only theoretical framework for SPPs scattering modeling, but also

experimentally demonstrated SPPs scattering have been reported to date. To scatter SPPs, patterned Au nano-bumps, grating in the metal film, and a nano-patterned dielectric overlayer are employed. Referring to Chang and et al. [12], SPPs manipulation by scattering is demonstrated using nano-bumps fabricated on 30-nm-thick Au thin film. For the nano-bumps on the Au thin film, the femtosecond-laser direct-writing technique is used. It exhibits that by precisely controlling the size of the nano-bumps, and the interspacing among nano-bumps, the interference patterns of the radiating scattered waves converted from SPPs are possibly designed in a preferred way. It is also proposed that using grating in a metal film is also possible to out-couple SPPs. The work done by Bolger [25] represents that SPPs can be either excited or out-coupled depending on the size of the gratings fabricated on the metal film. It employs the grating structure to observe amplified spontaneous emission of SPPs experimentally. At last, a nano-patterned dielectric over-layer implemented on the metallic cathode of a top-emitting organic emitting diode is reported to reduce substantially the loss incurred by the surface plasmon mode [26]. A nano-patterned dielectric over-layer is placed on the thin metallic cathode for index matching to enhance the coupling between each SPPs mode in each side of the cathode. The microstructures patterned on the dielectric over-layer, and then, act as like a scatterer to the coupled SPPs, recovering the loss from the surface plasmon mode. This research exhibits that for a thin metallic platform for SPPs mode, placing an index-matching layer with microstructures is the one of the efficient method for the SPPs manipulation based on scattering.

Speaking of SPP modes in OLEDs, a method is demanded to reduce the loss

resulting from the SPP modes. The unintentional excitation of SPP modes in OLEDs is still considered as a crucial problem that impinges the external quantum efficiency (EQE) of OLEDs, though the efficiency of OLEDs has been improved significantly. Active research has been proceeded to out-couple SPPs in OLEDs to recover the loss, thus to increase EQE. Since excitation of SPPs is dependent on the orientation of the emitting molecules, controlling the orientation of the molecules is proposed as a solution [27]. Another reported method for out-coupling SPPs is increasing the distance between the emitting molecules and the metallic electrode by adding a buffer layer or thickening a charge transport layer to reduce the excitation efficiency of SPPs [28]. It is also proposed by Meyer [29], and Kim [30] that metal electrode-free OLEDs could be an alternative way to avoid the loss problem caused by SPP modes since SPPs result from coupling between charges in a metal and photons.

In this section, we have summarized preceding research for SPPs manipulation. For plasmonic integrated circuits or all-optical chips to be realized, SPPs modulation including SPPs guiding, manipulating, and scattering is in demand for active research. A well-designed and investigated SPPs modulation structure could indulge the demand and solve the remained problem, such as the loss incurred by the SPP modes in OLEDs.

3. Results and Discussion

3.1 Simulation structure and method

The FEM based simulation tool (COMSOL) [31] is employed to numerically investigate SPP-scattering properties of a dielectric nanocube embedded in a metal layer. The FEM based simulation is a powerful methodology to analyze electromagnetic waves interacting with complex structures. Moreover, it is capable of not only three-dimensional calculations (if computation power is enough), but also investigating nano-scaled phenomena. Figure 3.1.1 shows the schematic diagrams of the FEM simulation structure in three- [Fig. 3.1.1(a)] and two-dimensional views [Fig. 3.1.1(b)], which is used in this study for numerical analyses of SPP scattering by a dielectric (TiO_2) nanocube embedded in a metal layer (Ag). The scattering-analysis formalism in COMSOL is utilized to excite SPPs propagating along a planar metal–dielectric interface as background fields using Eqs. (2.7), (2.9), and (2.10). In order to define the simulation domain and minimize the boundary reflection, the perfectly matched layer [32] is used to enclose the domain. SPPs corresponding to the visible range in vacuum (visible SPPs) are excited from the left in the simulation domain as shown in Fig. 3.1.1, while a single TiO_2 nanocube is entirely embedded in the metal at the center of the simulation structure away from the metal–dielectric interface by a distance of 10 nm [as indicated in Fig. 3.1.1(b)]. The excited SPPs from the left interact with the embedded nanocube in the metal layer as they propagate. SPPs are scattered by the embedded nanocube and then the scattered waves of SPPs are numerically investigated. Finite-sized

TiO₂ nanocubes with an edge length w of 100, 80 and 60 nm are examined. For the material properties of both the metal layer (Ag) [33] and the embedded nanocube (TiO₂) [34], frequency-dependent relative permittivity are used [Fig. 3.1.2]. The relative permittivity value of the dielectric media adjacent to the metal layer is assumed as a constant and real value ($\epsilon_{\text{die.media}} = 1.7^2$).

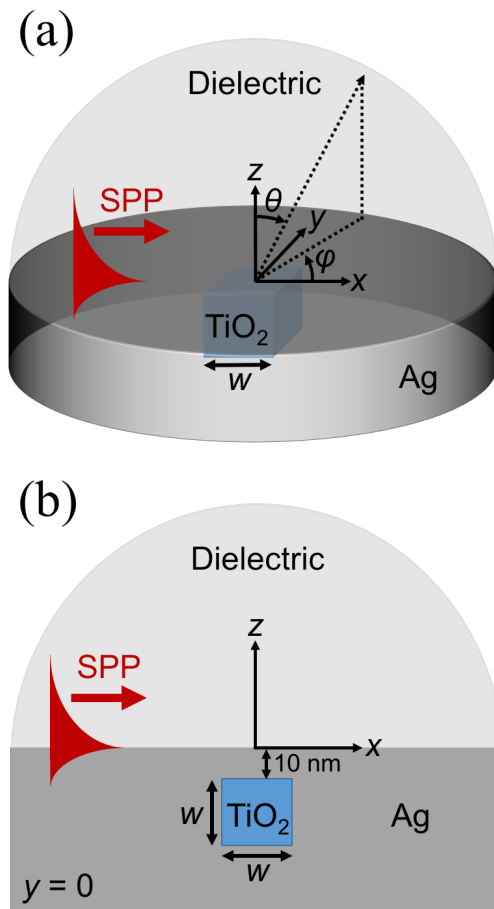


Figure 3.1.1 Schematic diagrams of the simulation structure showing that SPP (red) is excited from the left to the right, propagating along the x axis, while a TiO_2 nanocube ($w = 100, 80, \text{ or } 60 \text{ nm}$) is embedded in the Ag layer. The structure is shown in three-dimensional (a) and two-dimensional (b) views, where θ and φ represent the polar and azimuthal angles, respectively.

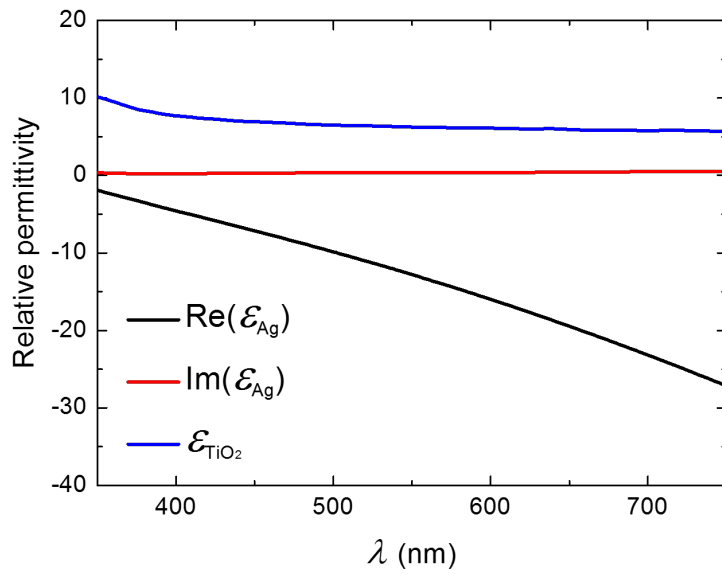


Figure 3.1.2 Frequency-dependent relative permittivity (ϵ) of the metal layer (Ag) and the embedded dielectric nanocube (TiO_2) as a function of a wavelength in vacuum (λ) used in this study.

To numerically investigate SPP-scattering properties of a dielectric (TiO₂) nanocube embedded in a metal layer (Ag) as shown in Fig. 3.1.1, cross sections of scattering (into the far field) and absorption, far-field scattering patterns, reflectance, and transmittance are calculated for incident SPP waves whose wavelengths are in the visible range employing FEM COMSOL simulations.

3.2 Scattering of surface plasmon polaritons into the far field

Figure 3.2.1 represents numerically calculated cross section of SPPs scattering into the far field of the dielectric nanocube embedded in the metal layer (S_{sca}), clearly showing that at specific wavelengths, the scattering of SPPs into the far field by the embedded nanocube is significantly increased. In this study, a modified definition of cross section is used since SPPs are electromagnetic waves confined to the metallic surface. The S_{sca} is calculated from the total power of the scattered waves into the far field divided by the incident power of SPPs per unit length, representing a quantitative characteristic of the embedded nanocube for SPP scattering into the far field. Since the incident SPP waves are confined to the metal–dielectric interface, the power of the scattered waves to the far field is obtained by surface integral of time-averaged Poynting vector of the scattered waves on a plane parallel to the metal surface ($z = 0$ nm), located at $z = 20$ nm. For the incident power of SPP waves, it is calculated from surface integral of time-averaged Poynting vector of the incident SPPs on the yz -plane bisecting the nanocube, divided by the total length of the simulation domain in

y-axis (= 1 μm).

It is shown that the scattering cross-section is dependent on both the wavelength of the incident SPPs and the size of the embedded nanocube. The highest S_{sca} peak is blue-shifted by 40 nm per each decrease in the size of the embedded nanocube ($\Delta w = 20$ nm), indicating that by precisely controlling the size of the embedded nanocube, it is capable of tuning the scattering (to the far field) property of this embedded-nanocube structural system and scattering SPP waves selectively and efficiently. The maximum S_{sca} of 89.6 nm at $\lambda = 680$ nm (λ_1), 61.5 nm at $\lambda = 640$ nm, and 40.0 nm at $\lambda = 600$ nm are observed in the cases of $w = 100$, 80, and 60 nm, respectively, where λ is the wavelength of a SPP wave in vacuum.

Particularly, in the case of $w = 100$ nm, other prominent S_{sca} peaks with higher frequencies than that of the highest S_{sca} peak found are also observed at $\lambda = 640$ (λ_2) and 540 nm (λ_3). Similarly, in the cases of $w = 80$ and 60 nm, two S_{sca} peaks are also observed with higher frequencies at $\lambda = 600$ and 520 nm (for $w = 80$ nm) and at $\lambda = 570$ and 500 nm (for $w = 60$ nm). These S_{sca} peaks also show blue-shift as the size of the embedded nanocube decreases, suggesting a resonance characteristic of this embedded nanocube system. To discuss of a relation between the scattering properties and possible resonance properties of the system, the distribution of surface charge densities of the embedded nanocube and electric field profiles are investigated.

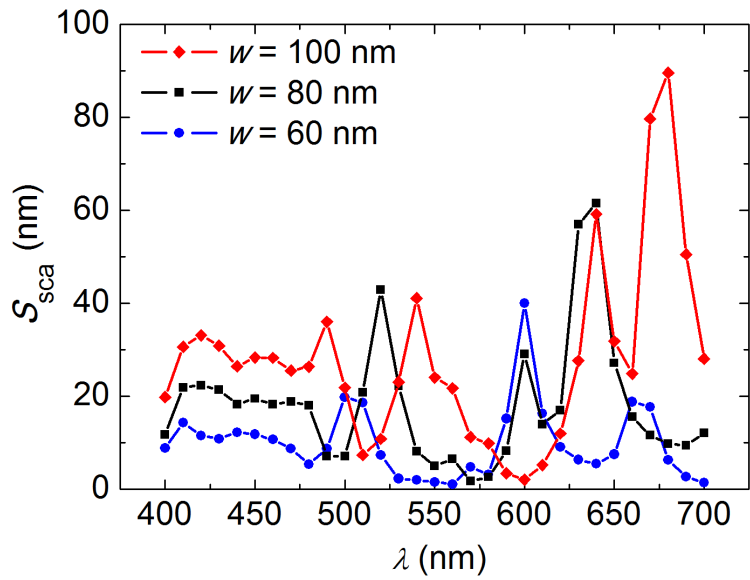


Figure 3.2.1 The S_{sca} spectra of the embedded nanocube with $w = 100, 80,$ and 60 nm as a function of λ .

Figure 3.2.2(a) shows the surface charge density (σ) distribution on the nanocube surfaces, which is calculated from the electric fields E at $\lambda = 680$ nm (λ_1), the condition resulting in the highest S_{sca} peak in the case of $w = 100$ nm. Together with the σ distribution and the E_x profile, where E_x is the x -component of electric fields, plotted in the xz -plane bisecting the embedded nanocube shown in Fig. 3.2.2(c), it is suggested that a mode with a dipolar plasmonic feature is apparently excited in the embedded nanocube, where charges of opposite polarities are induced on the left and right faces of the nanocube at $x = -50$ and 50 nm, respectively. The color saturation in some areas on the edges in Fig. 3.2.2(c) is attributed to the adjustment of the color scales for clear visualization of the field distribution. In order to verify the excitation of a plasmonic resonant mode in the embedded nanocube, eigenmodes of this embedded nanocube system are calculated using the eigenfrequency solver in COMSOL. Figure 3.2.2(b) shows the the σ distribution on the nanocube surfaces corresponding to an eigenmode found at $\lambda = 674$ nm, which is very similar to that shown in Fig. 3.2.2(a). Specifically, the two faces normal to the x -axis have surface charges with opposite polarities in both cases, with the σ distribution on each face induced with a single polarity only, confirming that the S_{sca} peak at λ_1 [Fig. 3.2.1] occurs due to excitation of this mode, hereafter referred to as the dipolar-like plasmonic mode. Because of this dipolar-like features, the coupling efficiency of this resonant mode with radiating modes is expected to be high [35], which is consistent with the fact that the S_{sca} peak at λ_1 is the highest peak in the SPP range.

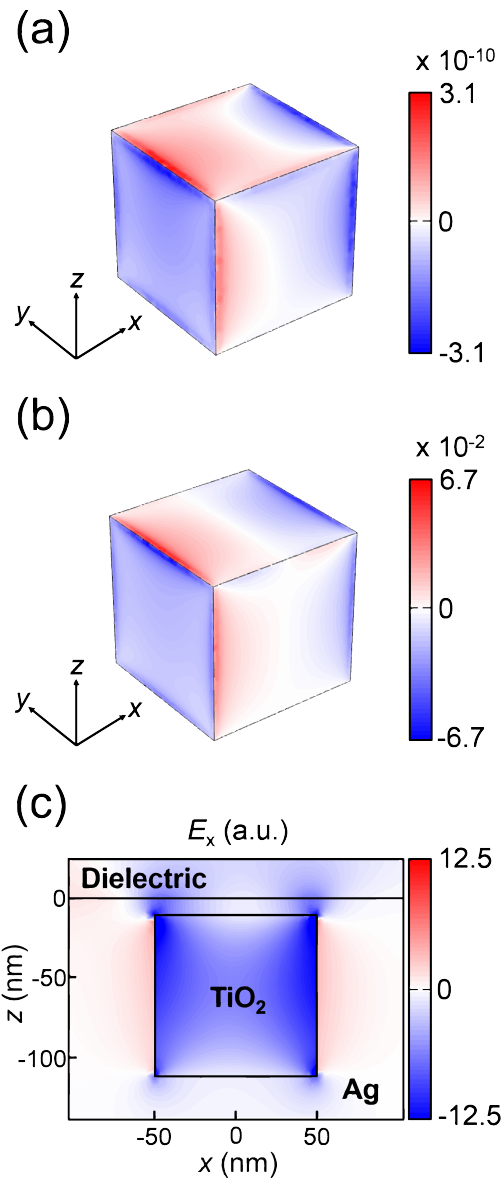


Figure 3.2.2 The surface charge densities (σ) distribution (a) and E_x field profile (c) of the 100-nm nanocube corresponding to the S_{sca} peak at $\lambda = 680$ nm (λ_1). In (b), the σ distribution over the embedded nanocube of the eigenmode found at $\lambda = 674$ nm.

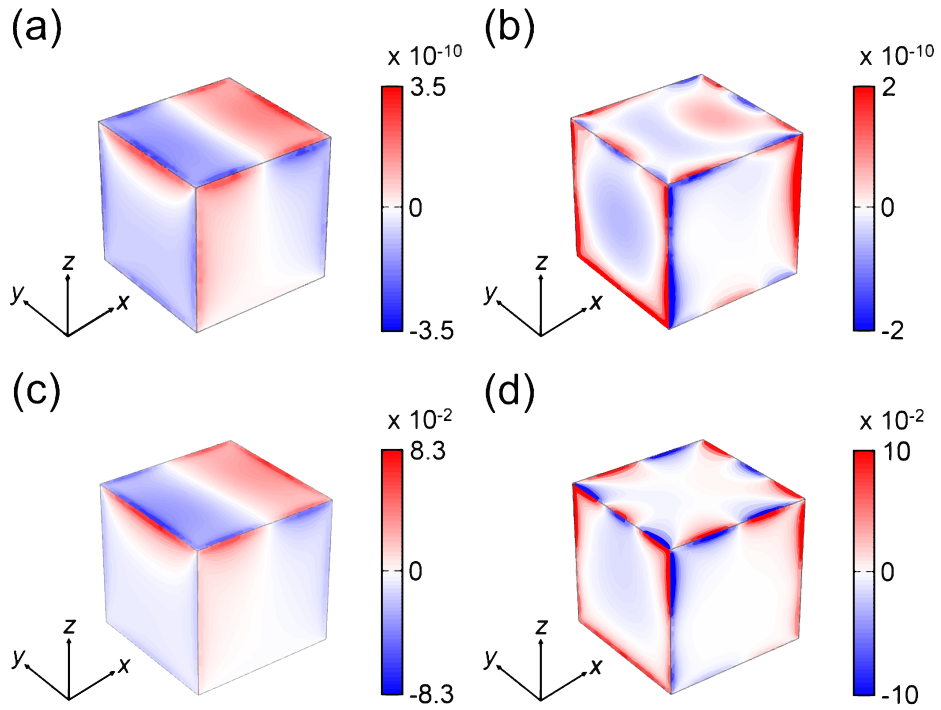


Figure 3.2.3 The surface charge densities (σ) distribution of the 100-nm nanocube corresponding to the S_{sca} peaks at $\lambda = 640$ (λ_2) and 540 nm (λ_2) are shown in (a) and (b), respectively. In (c) and (d), the σ distributions corresponding to the eigenmodes found at $\lambda = 634$ and 539 nm are shown, respectively.

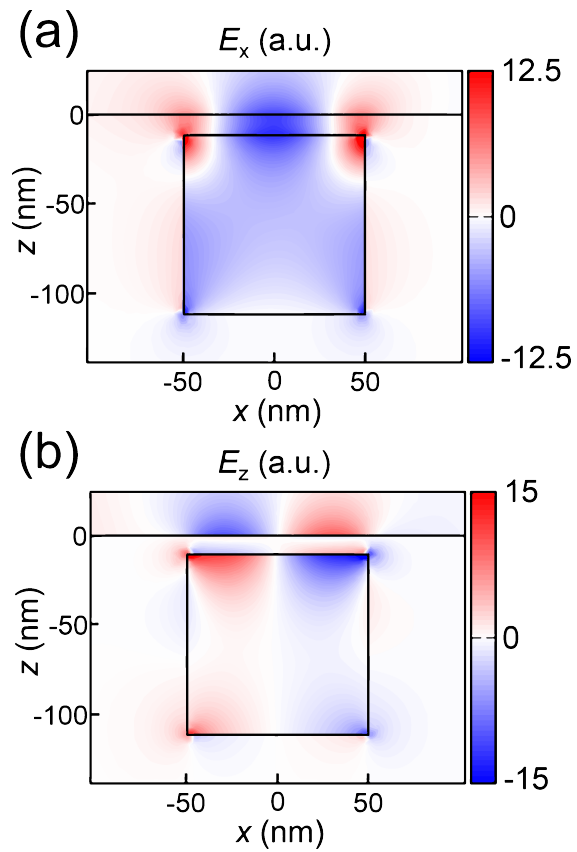


Figure 3.2.4 The E_x (a) and E_z (b) field profiles of the 100-nm nanocube for $\lambda = 640$ nm (λ_2), where a S_{sca} peak is found.

Close resemblance of the σ distributions of the embedded nanocube corresponding to the S_{sca} peaks, in the case of $w = 100$ nm, at $\lambda = 640$ nm (λ_2) and $\lambda = 540$ nm (λ_3), shown in Figs. 3.2.3(a) and 3.2.3(b), respectively, to those of eigenmodes found at $\lambda = 634$ [Fig. 3.2.3(c)] and 539 nm [Fig. 3.2.3(d)], which are close to λ_2 and λ_3 , respectively, is observed, indicating that the S_{sca} peaks at λ_2 and λ_3 occur due to resonant excitation of the respective eigenmodes as well. For the mode at λ_2 , referred to as the 1st higher mode, unlike the dipolar-like mode, each of the two faces normal to the x -axis has charges of both negative and positive polarities with one nodal line, which decreases the dipolar-like feature and, therefore, results in decreased S_{sca} compared to the dipolar-like mode. Furthermore, the E_x and E_z profiles, where E_x and E_z represent the x - and z -components of the electric fields, depicted in the xz plane bisecting the embedded nanocube are shown in Figs. 3.2.4(a) and 3.2.4(b), respectively, indicating that the electric field distribution near the 10-nm-thick Ag layer on the embedded nanocube is with the σ distributions on the top ($z = 0$ nm) and bottom ($z = -10$ nm) surfaces of the Ag layer nearly symmetric with respect to the plane at $z = -5$ nm. The field distribution resembles that of an asymmetric plasmonic slab waveguide mode in a dielectric–metal–dielectric multilayer structure [36].

In the case of the mode at λ_3 , referred to as the 2nd higher mode, the σ distribution on the surfaces of the embedded nanocube is strongly concentrated near the edges, and has much higher spatial frequency components, with more nodal lines compared to the other two modes, which is consistent with the fact

that this mode has a higher eigenfrequency [Fig. 3.2.3(d)]. Relatively weak similarity between Fig. 3.2.3(b) and 3.2.3(d) compared to the other two cases is likely due to weak coupling between this mode with high spatial frequency field components and the incident SPP wave.

The prominent S_{sca} peaks observed for $w = 80$ (black squares) and 60 nm (blue circles) in the S_{sca} spectra can also be explained by resonant excitation of the dipolar-like, 1st higher, and 2nd higher modes shown in Figs. 3.2.2(b), 3.2.3(c), and 3.2.3(d). In these cases, the resonant modes occur at shorter wavelengths due to smaller sizes of the embedded nanocube. For both cases of $w = 80$ and 60 nm, the σ distribution induced by incident SPP waves that maximize S_{sca} [Fig. 3.2.5(a) at $\lambda = 640$ nm and Fig. 3.2.5(b) at $\lambda = 600$ nm, respectively] are very similar to that of the dipolar-like plasmonic mode shown in Fig. 3.2.2(b). Furthermore, at the next two peaks observed at shorter wavelengths ($\lambda = 600$ and 520 nm for $w = 80$ nm, and $\lambda = 570$ and 500 nm for $w = 60$ nm), the σ distributions [Figs. 3.2.5(c) to 3.2.5(f)] very closely resemble those of the corresponding higher modes shown in Figs. 3.2.3(c) and 3.2.3(d), except for the S_{sca} peak at $\lambda = 500$ nm in the case of $w = 60$ nm [Fig. 3.2.5(f)]. In the case of $w = 60$ nm for $\lambda = 500$ nm, although charges are concentrated on the edges, similar to the cases of $w = 80$ and 100 nm, a different σ distribution is observed on the nanocube faces, which is instead similar to that associated with the 1st higher mode. The color saturation near the edges in Figs. 3.2.3(b) and (d), Figs. 3.2.4(a) and (b), and Figs. 3.2.5(e) and (f) is attributed to the adjustment of the color scale.

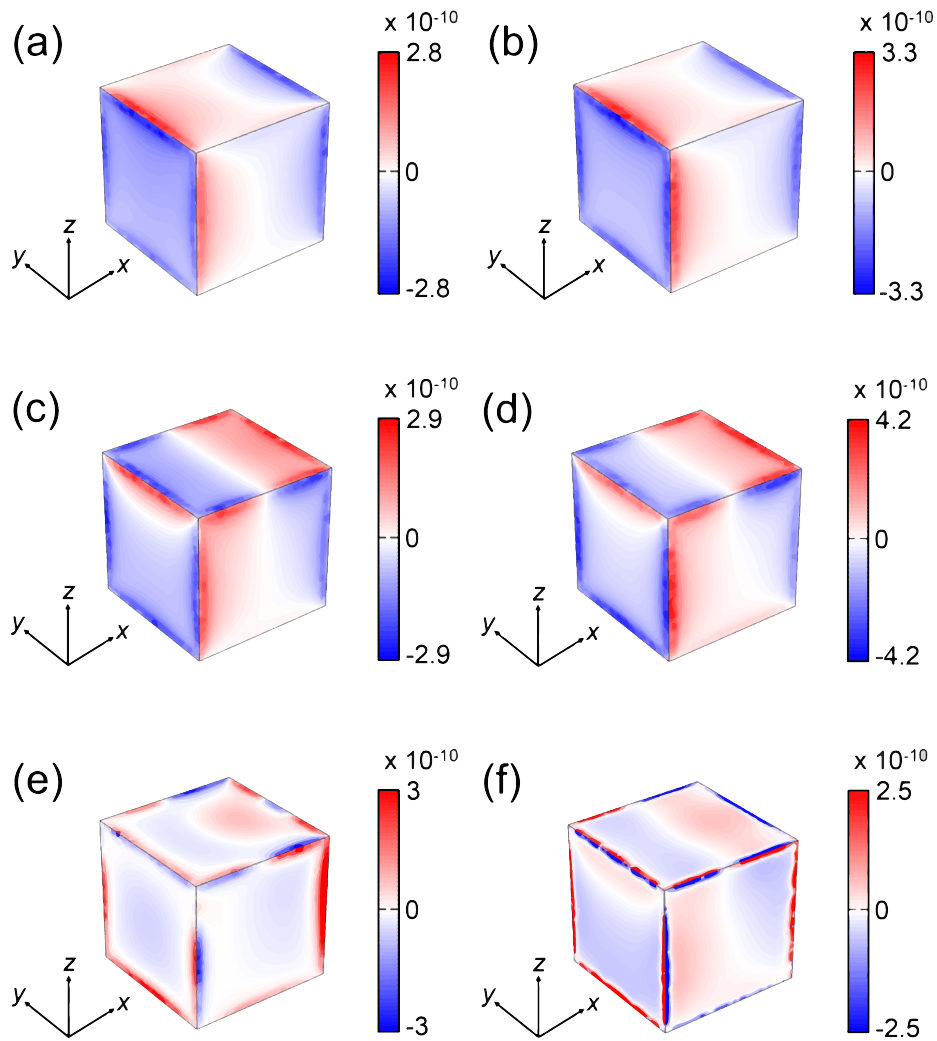


Figure 3.2.5 The distribution of surface charge densities (σ) of the embedded nanocube with $w = 80$ and $w = 60$ when the S_{sca} peaks arise: (a) $w = 80$ nm and $\lambda = 640$ nm (the dipolar-like mode), (b) $w = 60$ nm and $\lambda = 600$ nm (the dipolar-like mode), (c) $w = 80$ nm and $\lambda = 600$ nm (the 1st higher mode), (d) $w = 60$ nm and $\lambda = 570$ nm (the 1st higher mode), (e) $w = 80$ nm and $\lambda = 520$ nm (the 2nd higher mode), and (f) $w = 60$ nm and $\lambda = 500$ nm (the 2nd higher mode).

For $w = 60$ nm, an additional peak of S_{sca} is observed at $\lambda = 660$ nm longer than the wavelength at which the dipolar-like plasmonic mode is excited. This S_{sca} peak is due to excitation of a mode found at $\lambda = 675$ nm, which was not found in the cases of $w = 80$ and 100 nm in the wavelength range examined, since the σ distribution associated with this mode, shown in Fig. 3.2.6(b), is almost identical to that calculated from the E field in the scattering simulation, shown in Fig. 3.2.6(a). Like the 1st higher mode, this mode features a field distribution of an asymmetric plasmonic slab waveguide mode, as is confirmed by the E_x and E_z profiles shown in Figs. 3.2.6(c) and 3.2.6(d). The color saturation near the edges in Figs. 3.2.6(c) and (d) is attributed to the adjustment of the color scale for clear visualization of the field distribution. In this case, the σ distributions on the top and bottom surfaces of the 10-nm-thick Ag layer, consisting entirely of a same, single polarity, are composed of lower spatial frequency components than those of the 1st higher mode, consistent with its smaller eigenfrequency.

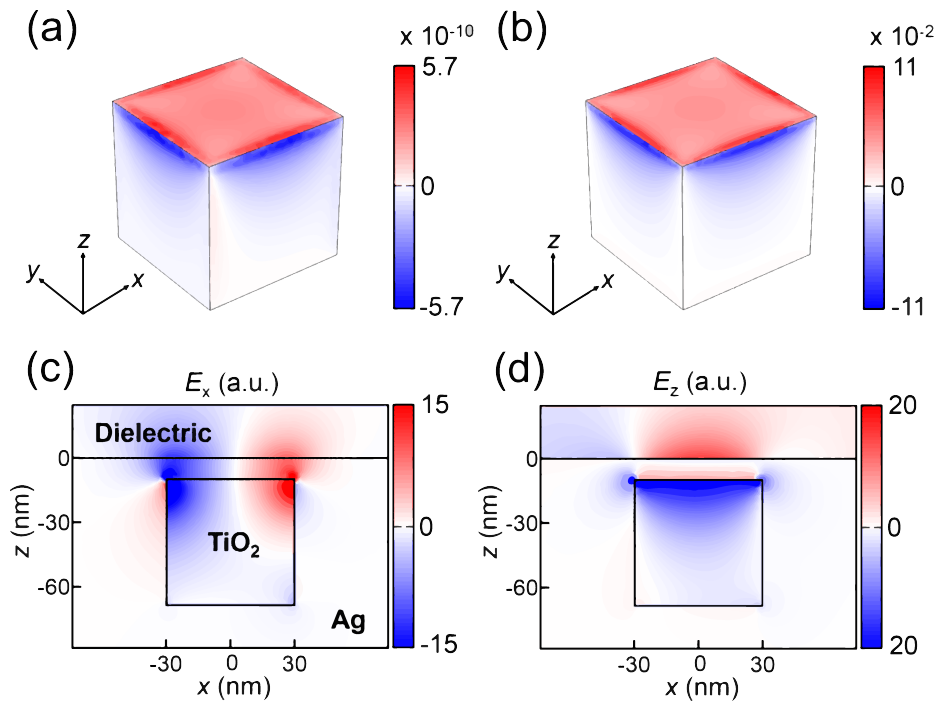


Figure 3.2.6 Characteristics of the additional resonant mode in the 60-nm nanocube. The distribution of surface charge density (σ) for $\lambda = 660$ nm is shown in (a), which is obtained from the SPP scattering simulation; the σ distribution corresponding to the eigenmode found at $\lambda = 675$ nm via the eigenmode calculation is shown in (b). The E_x and E_z profiles in this case are also shown in (c) and (d), respectively.

Figure 3.2.7 shows the normalized values of $|\mathbf{E}_{\text{sca}}|^2$ on the surface of the dielectric hemisphere, where \mathbf{E}_{sca} is the complex scattered electric fields, representing the differential scattering cross sections of the nanocube, where θ and φ are the polar and azimuthal angles defined in Fig. 3.1.1. To include only the SPP waves scattered and then propagating away from the metal surface in the calculation for the scattering patterns, i.e., to exclude the near fields of the nanocube, and transmitted and reflected SPP waves still bound at the Ag–dielectric interface, the radius of the hemisphere was increased to 2 μm and only the region with $\theta \leq 75^\circ$ was considered.

Figures 3.2.7(a) to 3.2.7(c) are the far-field scattering patterns for $w = 100$ nm corresponding to the three S_{sca} peaks associated with the dipolar-like, 1st higher, and 2nd higher modes, respectively. The results for $w = 80$ nm and 60 nm are not shown since the patterns associated with a same mode are almost identical to one another regardless of w . Also shown is the far-field scattering pattern corresponding to the additional peak at $\lambda = 660$ nm for the case of $w = 60$ nm [Fig. 3.2.7(d)].

Since the strong scattering of SPP waves results from resonant oscillation of charges on the surfaces of the nanocube, whose distribution is found to be different in each case of the four eigenmodes, as shown in Figs. 3.2.2(a), 3.2.3(a), 3.2.3(b), and 3.2.6(a), the scattering pattern associated with each eigenmode has a unique angular distribution: incident SPP waves with $\lambda = 680$ (for $w = 100$ nm), 640 (for $w = 80$ nm), and 600 nm (for $w = 60$ nm) exciting the dipolar-like plasmonic mode are scattered mostly in the direction normal to

the metal surface as shown in Fig. 3.2.7(a). When the 1st higher mode is excited at $\lambda = 640$ (for $w = 100$ nm), 600 (for $w = 80$ nm), and 520 nm (for $w = 60$ nm), the most of scattering points toward the forward direction, with maximum scattering toward the direction of $(\theta, \varphi) = (52^\circ, 0^\circ)$ [Fig. 3.2.7(b)]. For the case of the 2nd higher mode excited at $\lambda = 540$ (for $w = 100$ nm), 520 (for $w = 80$ nm), and 500 nm (for $w = 60$ nm), the most of scattering occurs toward the forward direction as well, with maximum scattering pointing to the direction of $(21^\circ, 0^\circ)$ [Fig. 3.2.7(c)]. Unlike the other cases, most scattered waves in the case of excitation of the additional mode shown in Fig. 3.2.6(a) are directed backwards with a much wider angular distribution in φ [Fig. 3.2.7(d)].

3.3 Absorption characteristics

Figure 3.3.1 shows the spectra of absorption cross section S_{abs} calculated for the three cases of $w = 100, 80,$ and 60 nm. Since the permittivity of the metal layer (Ag) in our study is complex, propagating SPP waves are absorbed in the metal layer. Therefore, to characterize the absorption resulting from the interaction with the embedded nanocube only, the absorption in the metal layer near the nanocube only needs to be considered. For this reason, S_{abs} is defined as the total power dissipated in the metal region with a thickness of 10 nm surrounding the embedded nanocube as shown in Fig. 3.3.2, divided by, as in the S_{sca} calculation, the incident SPP power per unit length in the y direction. As in Fig. 3.3.2, the thickness of 10 nm for the metal layer is sufficiently enough to include most of the power dissipated due to the embedded nanocube since the dissipated power arises within the region.

Overall, the S_{abs} spectra have peaks occurring at or near λ where peaks in S_{sca} are located. This is expected since excitation of an eigenmode causing strong scattering, leads to the concentration of the E field near the embedded nanocube. For $w = 100$ nm (red diamonds), the value of the S_{abs} peak at $\lambda = 670$ nm associated with the excitation of the dipolar-like plasmonic mode is found to be much smaller than that of the peak at $\lambda = 650$ nm attributed to the 1st higher mode, while the opposite is true for the S_{sca} spectrum. This can likely be rationalized by the fact that the dipolar-like plasmonic mode is expected to be very efficient in scattering of SPPs into the far field so that a larger portion of its extinction is attributed to scattering compared to the 1st higher mode. High

absorption across the broad region with $\lambda < 480$ nm is possibly due to eigenmodes with high frequencies that are closely spaced, although a mode analysis in this region was not performed.

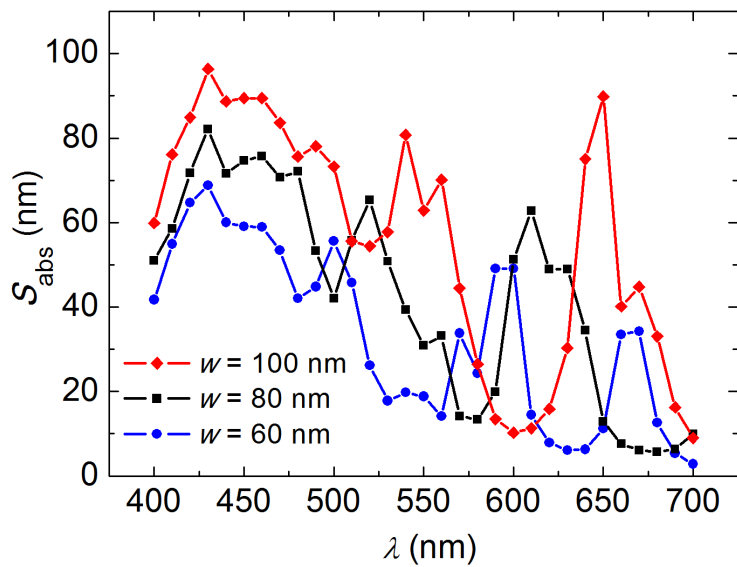


Figure 3.3.1 The S_{abs} spectra of the embedded nanocube with $w = 100, 80,$ and 60 nm as a function of λ .

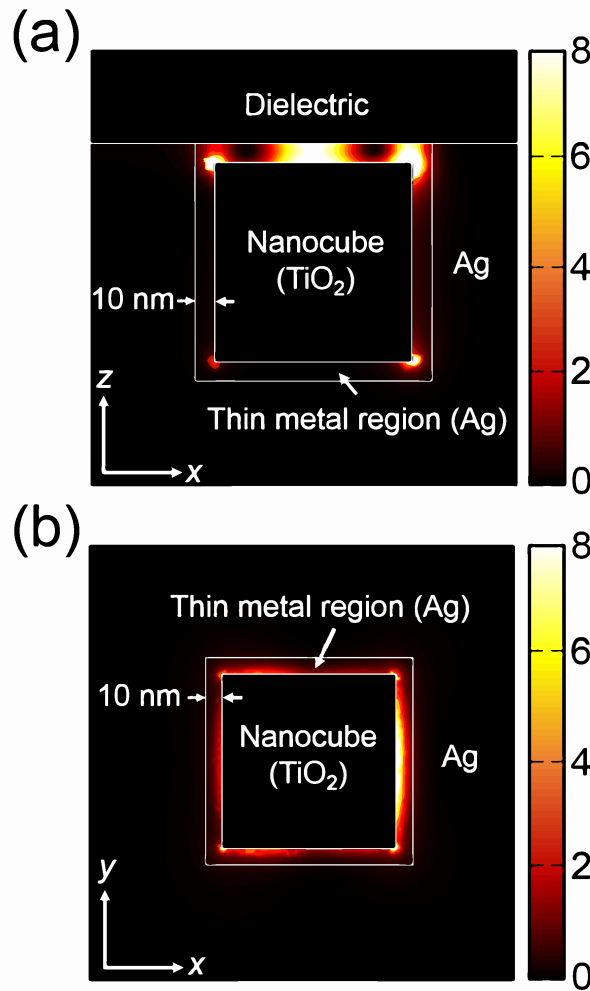


Figure 3.3.2 The dissipated power density inside the metal layer (Ag) including the embedded nanocube (TiO₂) and the thin metal region (indicated by the white arrow), which is considered in the absorption calculation, plotted in the xz -plane bisecting the nanocube (a) and in the xy -plane located at $z = -15$ nm (b) in the case of $w = 100$ nm and $\lambda = 650$ nm.

3.4 Reflection and transmission

In Fig. 3.4.1, the reflectance (R) and transmittance (T) spectra are shown, with the S_{sca} spectra included for comparison. Since the power of a SPP mode bound at a planar metal–dielectric interface is proportional to the component of the E field in the propagation direction [37], the E fields are monitored at two probe points to estimate R and T . Specifically, $R \cong |E_{\text{sca},x}|^2 / |E_{\text{inc},x}|^2$ is evaluated at $(x, y, z) = (-w/2 - 50 \text{ nm}, 0, 0)$, where $E_{\text{sca},x}$ and $E_{\text{inc},x}$ are the x components of the scattered and incident complex electric fields, respectively. Likewise, $T \cong |E_x|^2 / |E_{\text{inc},x}|^2$ is evaluated at $(w/2 + 50 \text{ nm}, 0, 0)$, where E_x is the x component of the total complex electric field: $E_x = E_{\text{sca},x} + E_{\text{inc},x}$. The locations of the left and right probe points were chosen to be 50 nm away from the left and right faces of the nanocube to obtain the approximate powers of the backward- and forward-scattered SPP waves, respectively, while excluding the near field of the nanocube.

It was found that the peaks in the R spectra (green) are located near the S_{sca} peaks, meaning that high reflection arises from enhanced back scattering of the incident SPP waves into backward propagating SPPs bound at the metal–dielectric interface by resonant excitation of the eigenmodes that give rise to the S_{sca} peaks. Figure 3.4.2 is the $|\mathbf{E}|^2$ distribution in the plane normal to the z -axis located at $z = 1 \text{ nm}$, where \mathbf{E} is the total complex electric field, when a SPP wave with $\lambda = 640 \text{ nm}$ is incident on the 100-nm nanocube, clearly showing the interference patterns resulting from the reflection and the E field intensity highly concentrated in the nanocube due to resonant excitation of the

1st higher mode. In contrast to R , the T spectra (blue) have local minima near the frequencies where the S_{sca} spectra have local maxima, and high values of T were obtained in the frequency regions where the values of S_{sca} and R are small. Interestingly, when a SPP wave with $\lambda = 680$ nm is incident on the 60-nm nanocube, T is found to exceed 1, indicating that the local field enhancement occurs in a region behind the nanocube, as shown in Fig. 3.4.3: Figure 3.4.3 shows the $|\mathbf{E}|^2 / |\mathbf{E}_0|^2$ distribution in the plane at $z = 1$ nm normal to the z axis, where \mathbf{E} and \mathbf{E}_0 are the total complex electric fields with and without the nanocube, respectively, and the black lines in Fig. 3.4.3 represent the boundaries of the regions in which $|\mathbf{E}|^2 / |\mathbf{E}_0|^2$ is larger than 1.1.

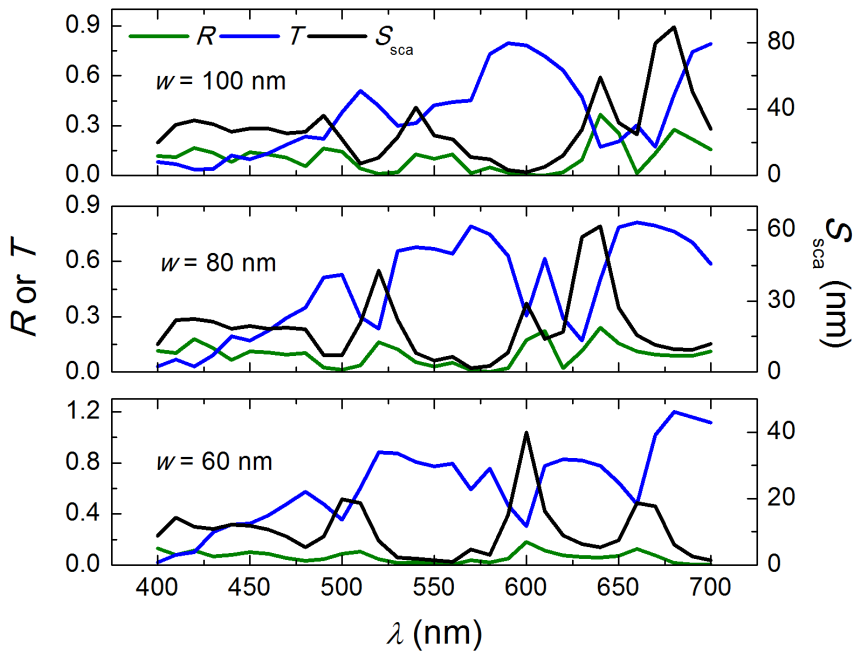


Figure 3.4.1 Calculated spectra of R (green) and T (blue) compared with the values of S_{sca} (black) of the embedded nanocube for $w = 100, 80,$ and 60 nm.

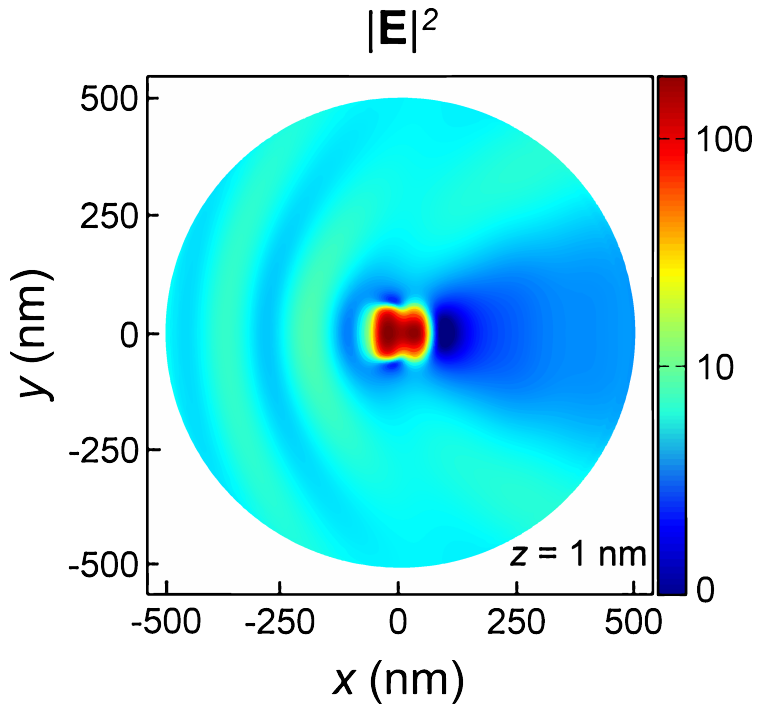


Figure 3.4.2 $|E|^2$ distribution (log scale) over the xy plane at $z = 1$ nm in the case of the maximum reflectance (when $w = 100$ nm and $\lambda = 640$ nm).

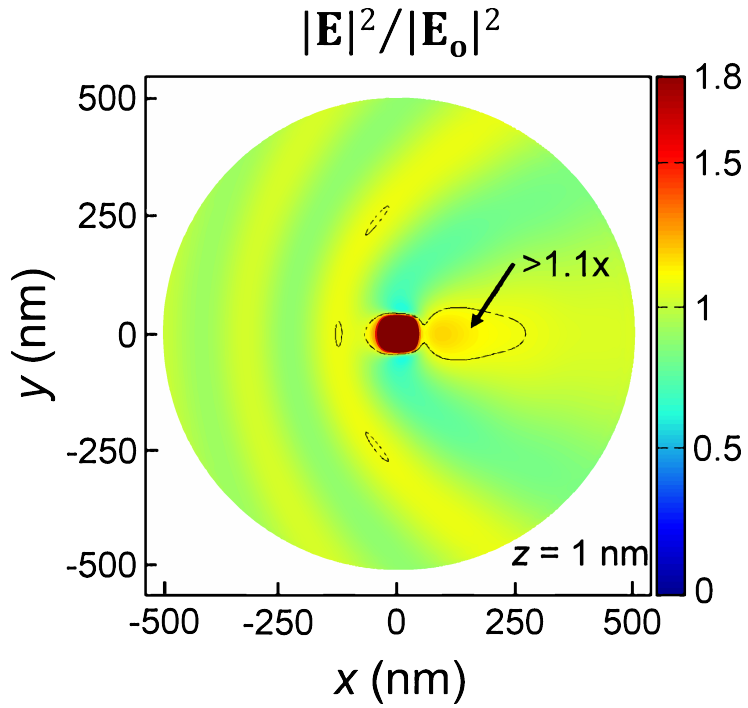


Figure 3.4.3 Local field enhancement ($|\mathbf{E}|^2 / |\mathbf{E}_0|^2$) on the surface of the metal layer due to the embedded nanocube with $w = 60$ nm at $\lambda = 680$ nm.

4. Conclusion

In this study, the numerical analyses of the SPP scattering at a planar metal–dielectric interface by a dielectric nanocube embedded in the metal layer are performed employing FEM simulations. In each case of the embedded nanocube with a different edge length, $w = 100, 80, \text{ or } 60 \text{ nm}$, the prominent peaks in the S_{sca} spectrum are found to be due to excitation of different plasmonic resonant modes of this embedded nanocube system. The strongest scattering of SPP waves into the far field occurs when the dipolar-like plasmonic mode is excited, specifically in this study at $\lambda = 680, 640, \text{ and } 600 \text{ nm}$ for $w = 100, 80, \text{ and } 60 \text{ nm}$, respectively. Comparing to the dipolar-like plasmonic mode, two modes with higher eigenfrequencies, referred to as the 1st and 2nd higher modes, and the additional mode with lower eigenfrequency than that of the dipolar-like plasmonic mode are shown that they are less efficient in scattering of SPPs into the far field, resulting in S_{sca} smaller than those in the case of the dipolar-like plasmonic mode. The far-field scattering patterns corresponding to the S_{sca} peaks are also shown as dependent on the plasmonic modes associated with the peaks. The most of scattering due to the dipolar-like mode is directed toward the direction normal to the metal (Ag) surface. This numerical study may contribute to realize efficient SPPs scattering at a planar interface, which is demanded in areas of thin film spectroscopy and integrated plasmonic circuits. Furthermore, our simulation geometry not only represents a general case of scattering of SPPs confined at a planar metal–dielectric interface, but also is particularly relevant to a region near a metal electrode in

an OLED. It is known that in OLEDs, near-field coupling of excitons into SPP modes decreases the efficiency of devices. This problem may be overcome by scattering those SPP modes into the far field using dielectric nanocubes, which can be embedded in the top electrode by depositing them, preferably using a dry process, on a thin (~ 10 nm) metal layer constituting the top electrode, followed by deposition of a thick (~ 100 nm) layer of the same metal. For successful realization of this, further numerical studies including the effects of different orientations and shapes of the nanocubes, and distances between the nanocubes and the metal–dielectric interface, as well as experimental investigations, are necessary.

Bibliography

- [1] B. Wang and G. P. Wang, "Surface plasmon polariton propagation in nanoscale metal gap waveguides," *Opt. Lett.*, vol. 29, no. 17, pp. 1992–1994, 2004.
- [2] R. Charbonneau, N. Lahoud, G. Mattiussi, and P. Berini, "Demonstration of integrated optics elements based on long-ranging surface plasmon polaritons," *Opt. Express*, vol. 13, no. 3, pp. 977–984, 2005.
- [3] A. B. Evlyukhin, S. I. Bozhevolnyi, A. L. Stepanov, and J. R. Krenn, "Splitting of a surface plasmon polariton beam by chains of nanoparticles," *Appl. Phys. B Lasers Opt.*, vol. 84, no. 1–2, pp. 29–34, 2006.
- [4] T. Nikolajsen, K. Leosson, and S. I. Bozhevolnyi, "Surface plasmon polariton based modulators and switches operating at telecom wavelengths," *Appl. Phys. Lett.*, vol. 85, no. 24, pp. 5833–5835, 2004.
- [5] R. F. Oulton, V. J. Sorger, T. Zentgraf, R.-M. Ma, C. Gladden, L. Dai, G. Bartal, and X. Zhang, "Plasmon lasers at deep subwavelength scale," *Nature*, vol. 461, no. 7264, pp. 629–632, 2009.
- [6] X. Guo, J. Du, Y. Guo, and J. Yao, "Large-area surface-plasmon polariton interference lithography," *Opt. Lett.*, vol. 31, no. 17, pp. 2613–2615, 2006.
- [7] E. Lee, and C. Kim, "Analysis and optimization of surface plasmon-enhanced organic solar cells with a metallic crossed grating electrode," *Opt. Express*, vol. 20, no. S5, pp. A740–A753, 2012.

- [8] X. B. Shi, C. H. Gao, D. Y. Zhou, M. Qian, Z. K. Wang, and L. S. Liao, "Surface plasmon polariton enhancement in blue organic light-emitting diode: Role of metallic cathode," *Appl. Phys. Express*, vol. 5, no. 10, 102102, 2012.
- [9] A. L. Cullen, "Reflection from cylinder in surface-wave field," *Electron. Lett.*, vol. 11, no. 20, pp. 479–480, 1975.
- [10] A. M. J. Davis and F. G. Leppington, "The scattering of electromagnetic surface waves by circular or elliptic cylinders," *Proc. R. Soc. Lond. A.*, vol. 353, no. 1672, pp. 55–75, 1977.
- [11] F. Pincemin, A. A. Maradudin, A. D. Boardman, and J. J. Greffet, "Scattering of a surface plasmon polariton by a surface defect," *Phys. Rev. B*, vol. 50, no. 20, pp. 15261–15275, 1994.
- [12] C. M. Chang, M. L. Tseng, B. H. Cheng, C. H. Chu, Y. Z. Ho, H. W. Huang, Y. C. Lan, D. W. Huang, A. Q. Liu, and D. P. Tsai, "Three-dimensional plasmonic micro projector for light manipulation," *Adv. Mater.*, vol. 25, no. 8, pp. 1118–1123, 2013.
- [13] M. S. Kumar, X. Piao, S. Koo, S. Yu, and N. Park, "Out of plane mode conversion and manipulation of Surface Plasmon Polariton waves," *Opt. Express*, vol. 18, no. 9, pp. 8800–8805, 2010.
- [14] R. Meerheim, M. Furno, S. Hofmann, B. Lüssem, and K. Leo, "Quantification of energy loss mechanisms in organic light-emitting diodes," *Appl. Phys. Lett.*, vol. 97, pp. 253305-1–253305-3, 2010.
- [15] L. Novotny and B. Hecht, *Principles of Nano-optics* (Cambridge University Press, 2006).

- [16] T. Wang, B. Rogez, G. Comtet, E. Le Moal, W. Abidi, H. Remita, G. Dujardin, and E. Boer-Duchemin, “Scattering of electrically excited surface plasmon polaritons by gold nanoparticles studied by optical interferometry with a scanning tunneling microscope,” *Phys. Rev. B Condens. Matter Mater. Phys.*, vol. 92, no. 4, pp. 1–7, 2015.
- [17] R. H. Ritchie, “Plasma Losses by Fast Electrons in Thin Films,” *Phys. Rev.*, vol. 106, no. 5, pp. 874–881, 1957.
- [18] P. Berini, R. Charbonneau, N. Lahoud, and G. Mattiussi, “Characterization of long-range surface-plasmon-polariton waveguides,” *J. Appl. Phys.*, vol. 98, no. 4, 043109, 2005.
- [19] S. A. Maier, M. D. Friedman, P. E. Barclay, and O. Painter, “Experimental demonstration of fiber-accessible metal nanoparticle plasmon waveguides for planar energy guiding and sensing,” *Appl. Phys. Lett.*, vol. 86, no. 7, pp. 1–3, 2005.
- [20] J.-Q. Liu, L.-L. Wang, M.-D. He, W.-Q. Huang, D. Wang, B. S. Zou, and S. Wen, “A wide bandgap plasmonic Bragg reflector,” *Opt. Express*, vol. 16, no. 7, pp. 4888–4894, 2008.
- [21] A. Vakil and N. Engheta, “One-atom-thick reflectors for surface plasmon polariton surface waves on graphene,” *Opt. Commun.*, vol. 285, no. 16, pp. 3428–3430, 2012.
- [22] P. H. Lee and Y. C. Lan, “Plasmonic Waveguide Filters Based on Tunneling and Cavity Effects,” *Plasmonics*, vol. 5, no. 4, pp. 417–422, 2010.
- [23] A. Hosseini and Y. Massoud, “Nanoscale surface plasmon based resonator using rectangular geometry,” *Appl. Phys. Lett.*, vol. 90, no. 18, pp.

88–91, 2007.

[24] A. B. Evlyukhin and S. I. Bozhevolnyi, “Point-dipole approximation for surface plasmon polariton scattering: Implications and limitations,” *Phys. Rev. B - Condens. Matter Mater. Phys.*, vol. 71, no. 13, pp. 1–9, 2005.

[25] P. M. Bolger, W. Dickson, a V Krasavin, L. Liebscher, S. G. Hickey, D. V Skryabin, and a V Zayats, “Amplified spontaneous emission of surface plasmon polaritons and limitations on the increase of their propagation length.,” *Opt. Lett.*, vol. 35, no. 8, pp. 1197–1199, 2010.

[26] S. Wedge, J. A. E. Wasey, W. L. Barnes, and I. Sage, “Coupled surface plasmon-polariton mediated photoluminescence from a top-emitting organic light-emitting structure,” *Appl. Phys. Lett.*, vol. 85, no. 2, pp. 182–184, 2004.

[27] J. Frischeisen, D. Yokoyama, A. Endo, C. Adachi, and W. Brütting, “Increased light outcoupling efficiency in dye-doped small molecule organic light-emitting diodes with horizontally oriented emitters,” *Org. Electron. physics, Mater. Appl.*, vol. 12, no. 5, pp. 809–817, 2011.

[28] G. He, M. Pfeiffer, K. Leo, M. Hofmann, J. Birnstock, R. Pudzich, and J. Salbeck, “High-efficiency and low-voltage p-i-n electrophosphorescent organic light-emitting diodes with double-emission layers,” *Appl. Phys. Lett.*, vol. 85, no. 17, pp. 3911–3913, 2004.

[29] J. Meyer, T. Winkler, S. Hamwi, S. Schmale, H. H. Johannes, T. Weimann, P. Hinze, W. Kowlasky, and T. Riedl, “Transparent inverted organic light-emitting diodes with a tungsten oxide buffer layer,” *Adv. Mater.*, vol. 20, no. 20, pp. 3839–3843, 2008.

- [30] J. B. Kim, J. H. Lee, C. K. Moon, S. Y. Kim, and J. J. Kim, “Highly enhanced light extraction from surface plasmonic loss minimized organic light-emitting diodes,” *Adv. Mater.*, vol. 25, no. 26, pp. 3571–3577, 2013.
- [31] COMSOL, *COMSOL multiphysics user’s guide version 4.3*, 2012.
- [32] J. P. Berenger, “A perfectly matched layer for the absorption of electromagnetic waves,” *J. Comput. Phys.* vol. 114, no. 2, pp. 185–200, 1994.
- [33] S. Babar and J. H. Weaver, “Optical constants of Cu, Ag, and Au revisited,” *Appl. Opt.*, vol. 54, no. 3, pp. 477–481, 2015.
- [34] G. E. Jellison, L. A. Boatner, J. D. Budai, B.-S. Jeong, and D. P. Norton, “Spectroscopic ellipsometry of thin film and bulk anatase (TiO₂),” *J. Appl. Phys.*, vol. 93, no. 12, pp. 9537, 2003.
- [35] H. Wei, A. Reyes-Coronado, P. Nordlander, J. Aizpurua, and H. Xu, “Multipolar plasmon resonances in individual Ag nanorice,” *ACS Nano*, vol. 4, no. 5, pp. 2649–2654, 2010.
- [36] J. A. Dionne, L. A. Sweatlock, H. A. Atwater, and A. Polman, “Plasmon slot waveguides: Towards chip-scale propagation with subwavelength-scale localization,” *Phys. Rev. B*, vol. 73, no. 3, pp. 1–9, 2006.
- [37] F. Pincemin, A. A. Maradudin, A. D. Boardman, and J. J. Greffet, “Scattering of a surface plasmon polariton by a surface defect,” *Phys. Rev. B*, vol. 50, no. 20, pp. 15261–15275, 1994.

초록 (국문)

표면 플라즈몬 폴라리톤(surface plasmon polaritons, SPPs)이란, 금속 내부에 고유진동수로 운동하고 있는 전하들과 공명을 일으킬 수 있는 주파수와 운동량을 지닌 특정한 빛이 결합하여 금속 표면에 전하들의 집단적 전자 운동이 유발되고 그로 인해 금속 표면에 형성되는 전자기파를 말한다. 이러한 전자기파는 금속 표면을 따라 진행하며, 금속 표면(또는 금속-유전체 계면)에서 멀어질수록 전자기장의 세기가 기하급수적으로 감소하는 특징을 가진다.

SPPs는 이를 유발하는 전자기파보다 짧은 파장을 가지며 금속 표면에 국소적으로 형성되는 특징으로 인해, 회절 한계를 극복할 수 있으며, 나노스케일의 구조에서 신호 전달 체계를 구축할 수 있다. 또한, 금속 표면에 높은 전자기장의 세기를 가지면서 그 표면을 따라 형성되는 특징으로 인해, 나노구조체를 이용해 SPPs를 형성하여 광전자소자에서 빛의 흡수나 자발방출효율을 증가시킬 수 있다. 이러한 SPPs만의 특징들로 인해, SPPs는 준 파장대의 현미경과 리소그래피, 집적 플라즈모닉 회로, 그리고 유기광전자소자 분야에 활용되기 위해 많은 연구가 되고 있다. 하지만, SPPs를 효과적으로 활용하기 위해서는 SPPs를 다양하게 여기시키는 방법과 활용에 대한 연구뿐만 아니라, 금속 표면에

형성된 SPPs를 금속 표면을 벗어나 진행할 수 있는 원거리장(far-field)으로 변환하거나, SPPs 반사와 투과와 같이 파장에 따른 선택적 제어가 가능한 SPPs 제어 방법이 요구된다. SPPs를 금속 표면에서 산란시킨다면, SPPs를 금속을 벗어나 진행할 수 있는 전자기파로 바꾸는 것뿐만 아니라, 파장에 따른 반사율과 투과율 조절, 또한 산란된 SPPs에 특정한 방향성도 부여할 수 있어, SPPs를 정밀하고 다양하게 제어할 수 있다.

본 논문에서는 금속-유전체 계면에 가깝게, 금속(Ag) 내부에 삽입된 유전체 나노입자(TiO_2 로 이루어진 정육면체)를 활용하여 평면 금속 표면에서 SPPs를 산란시켰으며, 금속 내부의 삽입된 나노입자의 SPPs 산란 특성들을 3차원 유한요소법 시뮬레이션(COMSOL)을 통해 정량적으로 분석하였다. 금속 표면에 전자기적 모드로써 형성되어 표면을 따라 진행하는 SPPs는 금속 표면의 구조가 바뀌면 SPPs 모드가 유지되지 못하고, 표면을 벗어나 진행할 수 있는 전자기파(far-field), 반사된 SPPs나 또는 투과된 SPPs로 산란된다. 일반적으로 금속 표면에 그레이팅과 같이 평면 표면을 변화시켜 SPPs를 산란시키는 방법이 있다. 하지만, 금속 표면에 가깝게 금속 내부에 삽입된 높은 유전율의 유전체 나노입자를 활용하여, 금속 표면은 평평하게 유지하면서 SPPs 모드를 방해하거나 삽입된 나노구조물 사이즈에 따른 제어가 가능하다. 이 뿐만 아니라 다양한 크기의 나노입자를 이용하여

다양한 파장을 가지는 SPPs를 산란시킬 수 있다. 가시광 파장대에 해당하는 SPPs에 대해서 금속(Ag) 내부에 삽입된 한 변의 길이가 60 nm, 80 nm, 100 nm의 크기를 가지는 정육면체 형태의 유전체(TiO₂) 나노입자로 인한 SPPs의 원거리장으로의 산란, 원거리장의 산란 패턴, 반사와 투과를 각각의 파장에 따라 정량적으로 분석하였다. 더 나아가서, SPPs 산란에 대한 정량적인 분석 및 결과와 금속에 삽입된 정육면체 형태의 나노입자에서 존재하는 플라즈모닉 모드들과의 상관 관계에 대해 논하였으며, 이를 통해 삽입된 나노입자 크기를 변화시킴으로써 SPPs 산란 특성을 제어할 수 있는 사실과 더불어 삽입된 나노입자의 특정한 플라즈모닉 모드(쌍극자와 비슷하게 전하들이 진동하는 모드)가 상대적으로 다른 모드들보다 효율적으로 SPPs를 산란시키는 것을 확인하였다. 또한, 삽입된 나노입자의 플라즈모닉 모드를 선택적으로 활용함으로써 금속 표면에서 SPPs의 준 파장대 분포도 제어도 가능하다. 각각의 플라즈모닉 모드가 여기되었을 때, 다른 원거리장 산란 패턴(far field scattering pattern)이 생기는 것을 확인하였으며, 이는 모드를 선택함으로써 원거리장으로 산란되는 방향 또한 제어 가능한 것을 알 수 있다.

본 연구를 활용하여, 추후 정육면체 형태의 나노입자뿐만 아니라 다른 다양한 형태의 나노입자(또는 나노구조체)에 대해서도 SPPs 산란 특성에 대해 정량적인 분석이 가능할 것으로 기대된다. 더

나아가서, 여러 다른 나노입자의 크기, SPPs가 나노입자에 입사되는 각도, 또는 나노입자가 삽입되는 깊이와 같이 다양한 변수들에 대해서도 분석이 가능할 것이다. 이러한 분석들은 평면 금속-유전체 계면의 SPPs를 효율적으로 산란 및 제어할 수 있도록 기여할 것이고 이는 집적 플라즈모닉 회로의 성능을 개선시킬 수 있다. 또한, 유기발광소자에서 금속으로 이루어진 상부 전극에 알맞은 크기들로 이루어진 유전체 나노입자들을 삽입하여, 유기발광소자에서 생기는 SPPs를 산란시킬 수 있고 이로 인해 소자 내부에서 SPPs로 인한 효율 감소 문제를 해결할 수 있을 것으로 기대한다.

.....

주요어: 표면 플라즈몬 폴라리톤, 산란, 나노구조체, 유기발광소자

학번: 2014-24880